



## NRC Publications Archive Archives des publications du CNRC

### **Unsteady laminar to turbulent flow in a spacer-filled channel**

Mojab, S. M.; Pollard, A.; Pharoah, J. G.; Beale, S. B.; Hanff, E. S.

This publication could be one of several versions: author's original, accepted manuscript or the publisher's version. /  
La version de cette publication peut être l'une des suivantes : la version prépublication de l'auteur, la version  
acceptée du manuscrit ou la version de l'éditeur.

For the publisher's version, please access the DOI link below. / Pour consulter la version de l'éditeur, utilisez le lien  
DOI ci-dessous.

#### **Publisher's version / Version de l'éditeur:**

<https://doi.org/10.1007/s10494-013-9514-4>

*Flow, Turbulence and Combustion*, 92, Feb, pp. 563-577, 2014-02-01

#### **NRC Publications Record / Notice d'Archives des publications de CNRC:**

<https://nrc-publications.canada.ca/eng/view/object/?id=8da1831e-08a1-4fc0-bfbb-d073102f54ee>

<https://publications-cnrc.canada.ca/fra/voir/objet/?id=8da1831e-08a1-4fc0-bfbb-d073102f54ee>

Access and use of this website and the material on it are subject to the Terms and Conditions set forth at

<https://nrc-publications.canada.ca/eng/copyright>

READ THESE TERMS AND CONDITIONS CAREFULLY BEFORE USING THIS WEBSITE.

L'accès à ce site Web et l'utilisation de son contenu sont assujettis aux conditions présentées dans le site

<https://publications-cnrc.canada.ca/fra/droits>

LISEZ CES CONDITIONS ATTENTIVEMENT AVANT D'UTILISER CE SITE WEB.

#### **Questions?** Contact the NRC Publications Archive team at

PublicationsArchive-ArchivesPublications@nrc-cnrc.gc.ca. If you wish to email the authors directly, please see the  
first page of the publication for their contact information.

**Vous avez des questions?** Nous pouvons vous aider. Pour communiquer directement avec un auteur, consultez la  
première page de la revue dans laquelle son article a été publié afin de trouver ses coordonnées. Si vous n'arrivez  
pas à les repérer, communiquez avec nous à PublicationsArchive-ArchivesPublications@nrc-cnrc.gc.ca.



National Research  
Council Canada

Conseil national de  
recherches Canada

Canada

# UNSTEADY LAMINAR TO TURBULENT FLOW IN A SPACER-FILLED CHANNEL

S.M. Mojab<sup>1</sup>, A. Pollard<sup>1</sup>, J.G. Pharoah<sup>1</sup>, S.B. Beale<sup>1,2</sup>, E.S. Hanff<sup>2</sup>

<sup>1</sup> Department of Mechanical and Materials Engineering, Queen's University, Kingston, Canada,  
mojab@me.queensu.ca, pollard@me.queensu.ca, pharoah@me.queensu.ca

<sup>2</sup> National Research Council of Canada, Ottawa, Canada, steven.beale@nrc-cnrc.gc.ca,  
ernest.hanff@nrc-cnrc.gc.ca

## Abstract

*A combined numerical and experimental investigation has been carried out to study the flow behaviour in a spacer-filled channel, representative of those used in spiral-wound membrane modules. The fluid flow characteristics are presented for Reynolds numbers, ranging from 100 to 1000. It was found that the flow in this geometry moves parallel to and concomitantly rotate between the spacer filaments and the rate of rotation increases with Reynolds number. The flow mechanisms, transition process and onset of turbulence in a spacer-filled channel are investigated including the use of the velocity spectra at different Reynolds numbers.*

## 1. Introduction

Spiral wound membrane (SWM) modules are among the most common commercially available membrane modules, with major applications in reverse osmosis, water desalination and gas separation. Spacers are used in membrane modules to maintain a uniform gap between the membrane layers, as well as to promote flow mixing. Mixing can suppress membrane fouling, and precipitate enhanced mass transfer through the membrane surfaces [1]. However, the presence of spacers as an obstacle to the flow through the channel also increases the pressure loss in the modules. In order to improve the performance of membrane modules, it is useful to investigate the hydrodynamic conditions inside these configurations.

Several experimental [1-4] and computational studies [5-10] have been conducted to investigate the effects of spacer geometry on flow behaviour within the passages of spacer-filled channels. Da Costa et al. [1] conducted experiments to measure pressure drop along spacer-filled channels. They tested seven commercially available feed spacers with different orientation of the spacer in the channel and filament spacing. In addition, they performed flow visualisation by injecting air bubbles and dye into the test section. Kang and Chang [2] conducted flow visualization studies for laminar flow between two impermeable parallel plates with spacers with different configurations; zigzag-type and cavity-type. They used ink as the flow tracer and a camera to capture the motion, and observed the formation of two main recirculation regions downstream and upstream of each filament. Gimmelshtein and Semiat [3] used particle imaging velocimetry (PIV) to measure velocity and estimate the magnitude of a mixing index (defined similar to a turbulence intensity) in order to estimate regions of enhanced mass transfer in a unit cell of a spacer-filled channel. They used a spacer with approximately thickness of 0.8mm. No permeation through the membrane walls was considered in the work. Santos et al. [4] experimentally investigated 12 different spacer structures (difference in filaments spacing and the number of longitudinal filaments) to measure pressure drop, and obtained good agreement between the experimentally-obtained and numerically-obtained values of the friction factor.

In addition to experimental studies, two-dimensional [5-7] and three-dimensional [8,9] CFD modeling of fluid flows in spacer-filled channels provided further insights of flow phenomena

taking place inside membrane modules. Geraldles et al. [5] studied incompressible laminar 2D flow in channels with ladder-type spacers. The authors investigated the influence of spacer geometric parameters on flow structure and friction factor. Cao et al. and Schwinge et al. [6,7] investigated the effect of three transverse filament arrangements; zigzag, cavity and submerged spacers, on flow behaviour. Karode and Kumar [8] carried out 3D CFD simulations in spacer-filled channels with several commercially available spacers (used by Da Costa et al. [1]). They concluded that for compact spacer designs with small pitch, the bulk of the fluid flows parallel to the spacer filaments; however for widely-spaced units, the bulk of the fluid follow a zigzag path, similar to that proposed by Da Costa et al. [1]. Li et al. [9] used 3D CFD simulations to optimize a ladder spacer geometry with circular filaments, based on calculations of mass transfer and power consumption in the channels. They simulated a unit cell and imposed periodic boundary conditions. They proposed geometric parameters (the distance between spacer filaments, the angle between the spacer filaments and the flow attack angle) for optimum spacer geometry.

The paper presents the results of a combined experimental and direct numerical simulation investigation of the laminar-to-turbulent flow regimes encountered in a spacer filled channel. The spacer consists of two layers of parallel rods that are aligned at  $45^\circ$  with respect to the flow streamwise direction. A schematic of the spacer geometry and a  $2 \times 2$  unit cell along with dimensions are illustrated in figure 1. As shown in this figure, all filaments are of equal diameter ( $d$ ) that is equal to half the channel height ( $h$ ).

The paper is laid out as follows. First, the experimental campaign is briefly described; this is followed by an overview of the DNS approach that enables the finer flow physic details to be uncovered, especially the turbulence spectra. The data obtained from these two approaches are then presented and discussed. Finally, conclusions are drawn from the work presented.

## 2. Experiments

The geometry used in this study is a scaled-up ( $10\times$ ) version of the CONWED-1 configuration, typical of industrial membrane spacers [1]. The spacer is composed of 42 cylindrical rods placed in two layers perpendicular to each other and aligned at  $45^\circ$  with respect

to the mean flow direction within a rectangular channel of  $900\text{mm} \times 320\text{mm} \times 20\text{mm}$ . The resulting test section consists of 30 by 9 'unit cells' in the streamwise and crosswise directions, respectively, see figure 2. The diameter of the rods is  $d = 10\text{mm}$  thus the width of the channel becomes  $h = 20\text{mm}$  and the spacing between rods on a layer is  $l = 21.7\text{mm}$ .

A positive displacement lobe pump circulated the test fluid through a heat exchanger, test-section and reservoir tank. The temperature of the fluid was accurately controlled by means of a combined heater/chiller unit that circulated a water-glycol mixture through the secondary loop of the heat exchanger. In the present setup, an optically clear light mineral oil (Penreco Drakeol 5) was used as the test fluid, as its refractive index can be adjusted through temperature control, to match that of the fused silica material used for the test section enclosure and internal spacers. The resulting elimination of optical distortion by the solid-spacer material permitted interrogation throughout the entire flow assembly.

Two-dimensional PIV measurements were obtained with the apparatus shown schematically in Figure 2. The test fluid was seeded with hollow glass spheres of 18 microns mean diameter and a density of  $600\text{ kg/m}^3$ , slightly less than that of the test fluid ( $830\text{ kg/m}^3$ ) thus preventing them from sinking to the bottom of the test section and obstructing the passage of the laser light sheet. A double-pulse Nd:YAG laser sheet ( $70\text{ mJ/pulse}$ , at  $532\text{ nm}$ ) parallel to the sides of the test section was applied from below to illuminate the particles and the scattered light is observed by means of a camera ( $1600 \times 1200$  pixels) oriented with its axis normal to the test section wall and rotated by  $45^\circ$  so that the edges of the image were aligned with the spacers. In order to maximize spatial resolution, the camera was placed such that only one unit cell was viewed with velocity fields being obtained every  $1\text{ mm}$  in the  $y$  direction.

The time delay between the two illumination pulses was selected such that the fastest particles would travel approximately  $1/4$  to  $1/3^{\text{rd}}$  the length of the interrogation window. 1500 pairs of images were continuously recorded at a sampling frequency of  $10\text{ Hz}$  at each of 19 equidistant planes. A second order cross-correlation technique [10] was used to analyse each pair of images with adaptive multi-pass algorithms [11] using interrogation windows starting from

128 × 128 pixels and ending with 32 × 32 pixels using 50% overlap. Data were obtained for Reynolds numbers (based on the hydraulic diameter  $d_h$  and the interstitial velocity  $u$  [1]) in the range of  $100 < Re < 1000$ .

### 3. Numerical Simulations

Direct numerical simulations for the three dimensional, time-dependent Navier–Stokes equations for an incompressible fluid were performed:

$$\frac{\partial u_i}{\partial x_i} = 0, \quad (1)$$

$$\frac{\partial u_i}{\partial t} + \frac{\partial(u_i u_j)}{\partial x_j} = -\frac{1}{\rho} \frac{\partial p}{\partial x_i} + \nu \frac{\partial^2 u_i}{\partial x_j \partial x_j} \quad (2)$$

where  $u_i$ ,  $p$  and  $\nu$  are the velocity components, pressure and kinematic viscosity, respectively.

The numerical solution of the Navier–Stokes equations was obtained using the open-source CFD code, openFOAM version 1.5 (2008). In order to accurately predict transport phenomena in a spacer-filled membrane module using CFD, it is crucial to select a suitable unit cell for general types of spacers [12]. An unstructured hexahedral mesh was created using a Cartesian mesh, which was refined by the octree method (Shephard and Georges 1991) in the vicinity of the walls, and fitted to the surface of the geometry. The mesh generation utility is supplied with OpenFOAM. The Grid Convergence Index as suggested by Roache [13] was performed at the highest Reynolds number in order to obtain the required grid resolution. Hence, the computational grid was constructed with 5.3 million cells (starting with a 216 000 cell uniform Cartesian mesh and refined in 3 octree levels). Figure 3 illustrates the mesh arrangement.

The flow is assumed to be periodic in the  $x$  and  $z$  directions, at 45 deg. to the mean flow. A mean pressure gradient along the direction of specified bulk velocity was added as a volumetric source term to the momentum equation Patankar et al. [14]. No-slip boundary conditions were imposed at the spacer and membrane walls. In the present study spatial discretization is based on

central differencing scheme for second order accuracy. This method was used due to its minimal numerical diffusion [15]. The PISO algorithm is employed to effect pressure-velocity coupling. In addition, the Crank–Nicholson method is used for time advancement. The time steps were chosen to ensure a Courant number of less than 0.7. The numerical simulations were processed in parallel on 50 CPUs (Intel XEON processors) and the total simulation time for each case was about 8 days.

#### 4. Presentation and Discussion of Results

Figure 4 depicts the sequence of transitions observed in typical instantaneous velocity fields (in  $m/s$ ) of PIV results at plane  $x$ - $z$  and  $y = h/4$ , as the Reynolds number is varied between 100 and 1000. Note that the black dashed lines plotted in this figure indicate the position of spacer filaments boundary at the lower layer of channel ( $y = -h/4$ ). It can be seen that the flow structure is notably altered with the variation of Reynolds number. At lower Reynolds numbers ( $Re = 100$  and  $200$ ) the flow is steady as will be confirmed shortly. By increasing the Reynolds number to 300 the steady flow shifts to a more varicose pattern. At higher Reynolds numbers ( $Re > 300$ ), the flow becomes increasingly unsteady with large flow structures, and by  $Re = 1000$ , the flow displays broader range of length scales and contains irregular structures.

Comparisons between numerical (CFD) and experimental (PIV) values of the time-average velocity magnitude along the unit cell centre line ( $x = 0, z = 0$  and  $y = -h/2$  to  $h/2$ ), are shown in Figures 5 for  $100 < Re < 1000$ . Since in PIV results, only two components of velocity were measured; for this comparison, only two components of the time-averaged velocity are used from CFD results. The time-averaged velocity profiles indicate good symmetry about  $y = 0$  and the agreement between the CFD and experiment results are in good agreement. However, these time-averaged data hide the underlying flow physics revealed by the instantaneous velocity fields provided in figure 4, and it is to the DNS results that attention is now turned.

Vector glyphs of the time-averaged tangential velocity field ( $\bar{U}_{yz} = [\bar{U}_y, \bar{U}_z]$ ) at a plane ( $x = 0, 0 < y < h/2$ ) in the upper channel-layer for Reynolds numbers 300 and 1000 are shown in figure 6.  $\bar{U}_y$  and  $\bar{U}_z$  are the time-averaged  $y$  and  $z$ -components of velocity, respectively. Some swirl-like



motions are visible in the main flow streams in the figure. For  $Re < 300$ , a counter primary clock-wise vortex between the spacer filaments is apparent. As the Reynolds number is increased beyond about 350, in addition to the primary vortex, a pair of clock-wise secondary vortices (secondary vortices) are also observed adjacent the regions of the spacer filaments and the membrane wall.

Streamlines of time-averaged velocity in the region of the vortex cores in the upper channel layer, are plotted in Figure 7. From this figure, it is qualitatively observed that the flow “corkscrews” along the  $x$ -direction; as it flows parallel to the spacer filaments in the upper channel layer. This circulation motion in the upper channel flow is induced by shear from the lower channel layer, where the flow is at 90 degrees, and vice versa. There is a significant increase in the amount of flow circulation in the unsteady flow regime. The pitch of the swirling motion can be estimated from the amount of streamline rotation illustrated in this figure. The swirl pitch is the length of one complete turn, measured parallel to the axis of the swirl motion. Note that the amount of streamline rotation illustrated in figure 7 is for  $2 \times 2$  unit cells. The swirl pitch for the primary vortex at  $Re < 300$  is found to be about  $24L$ , however in the unsteady regime this is about  $6L$ , i.e., means the flow completes one rotation after passing 6 filament spacing lengths ( $6L$ ). This indicates a significant increase in the amount of flow rotation in the unsteady flow regime. The swirl pitches for the secondary vortices, 2 and 3, at  $Re = 1000$  are  $4L$  and  $6L$  respectively.

Further insight into the different flow regimes in a spacer-filled channel flow can be gained by analysing the velocity time histories and spectra at different Reynolds numbers. The compensated velocity power spectral density (PSD) contours as a function of Strouhal number ( $St$ ) and history of the normalized velocity fluctuation magnitude ( $\dot{u}/u = (U - \bar{U})/u$ , where  $U$  is the instantaneous velocity,  $\bar{U}$  is the time-averaged velocity and  $u$  is the interstitial velocity) versus the normalised time ( $t^* = tu/h$ ) are shown in figure 8(a,b), at three locations ( $x = 0, z = 0$  and  $y = -h/4, 0, h/4$ ). The compensated spectra are defined as  $PSD \bullet f^{5/3}/u^2$ , where  $f$  is the velocity frequency, in  $Hz$ . An inertial sub-range is present if the  $Re$  is high enough to provide a broad spectrum of frequencies and if  $PSD \bullet f^{5/3}/u^2$  remains constant over a reasonable breadth of frequency (the so-called Kolmogorov -5/3 region). The Strouhal number is the non-dimensional



frequency, which is defined as  $St = fh/u$ .

At low Reynolds numbers flow ( $Re = 100$  and  $200$ ),  $\dot{u}/u$  display no oscillation with time and the PSD remains relatively flat. The flow in this range of Reynolds number is steady. By increasing the Reynolds number to  $250$ , oscillatory unsteady-periodic behavior is apparent in the flow. It should be noted that for flow at  $Re = 250$  and  $300$ , the amplitude of the oscillations at  $y = 0$  are much greater than at  $y = -h/4$  and  $y = +h/4$ , which indicates that the velocity oscillation contains more energy at the middle of the channel than elsewhere. The fluctuations at  $-h/4$  and  $+h/4$  have a  $180^\circ$  phase shift relative to each other. A base frequency  $f_o$  as well as some harmonics are readily apparent ( $f_o=16.79$ ,  $2f_o=32.96$ ,  $3f_o=49.13$ ,  $4f_o=65$  Hz) for  $Re = 250$  and ( $f_o=19.5$ ,  $2f_o=38.5$ ,  $3f_o=57.4$ ,  $4f_o=76.3$ ,  $5f_o=95.2$ ,  $6f_o=114.8$  Hz) for  $Re = 300$ . The Strouhal numbers associated with the predominant mode are  $St = 1.18$  and  $St = 1.15$  at Reynolds number  $250$  and  $300$ , respectively. Further increase in the Reynolds number ( $Re = 350$ ) causes the flow to transition from a flow with well-defined frequency extrema to one that displays more random behavior over a broad range of frequencies. For  $Re > 350$ , the flow becomes fully unstable. As is seen in figure 8 the inertial sub-range of compensated normalized PSD covers a wider  $f$  range at higher Reynolds number. It is maintained that the flow at  $Re = 1000$  may be considered to be the onset of a turbulent regime, based on the PSD diagram and the observation of flow structures from PIV results at this Reynolds number, see also figure 4.

To better understand the periodic flow behaviour at  $Re = 250$  and  $300$ , the normalized velocity fluctuations and magnitude are plotted at three locations ( $x = 0$ ,  $z = 0$  and  $y = -h/4, 0, +h/4$ ) in figure 9. At  $y = +h/4$ ,  $\dot{u}$  and  $\dot{u}_x$  are similar due to the predominant magnitude of the  $x$ -component of velocity in the upper channel layer: As previously mentioned, in the upper channel, the main flow stream moves parallel to the filaments in the  $x$ -direction. Conversely,  $\dot{u}$  and  $\dot{u}_z$  are similar at  $y = -h/4$ , in the lower channel. The predominant behaviour of  $\dot{u}_x$  and  $\dot{u}_z$  at upper and lower channel layer can be observed in figure 10. Figure 10 indicates the normalized mean velocity components and magnitude at three locations ( $x = 0$ ,  $z = 0$  and  $y = -h/4, 0, +h/4$ ) for  $Re = 250$  and  $300$ . The amplitudes of the velocity fluctuation components at  $y = 0$  are about one order of magnitude larger than those at the two other locations. This is due to the interaction

of two main orthogonal flow streams in the shear layer at the centre of the channel. All fluctuating velocity components wavelengths are similar at each location. There is no phase shift between the velocity fluctuations components at  $y = 0$  location; however, at the other two locations there is about  $45^\circ$  phase shift between  $\dot{u}_y$  and other velocity fluctuations components. This zero phase shift between velocity components at  $y = 0$  is due to the same contribution of velocity  $x$  and  $z$  components to the total velocity magnitude, as shown in figure 10. Comparison of the fluctuating velocity components at the two Reynolds numbers (fig. 9) indicates that their profiles deform and become asymmetric as Reynolds number approaches 300. Further increases in Reynolds number ( $Re > 300$ ) result in this unsteady-periodic behaviour turning into an irregular pattern. This feature needs further investigation.

## 5. Conclusion

The flow within spacer-filled channel passages has been studied experimentally and numerically. It was found that the main flow splits into two streams which move parallel to the spacer filaments with  $90^\circ$  direction difference to each other. These two streams interact at the centre-plane where they exchange momentum. This results in a shear layer interaction in this region. In addition, the  $90^\circ$  direction difference in the principal directions of the flow streams, results in the application of tangential forces on the two flow streams. These tangential forces cause secondary swirling motions in the main flow streams. Two counter clock-wise swirling flows (primary vortices) that rotate with the main flow streams i.e., parallel to the solid spacers, were observed in the upper and lower layers. In addition, four small clock-wise swirling motions (secondary vortices) were also observed at the corners of the channel/spacer regions for flow at  $Re > 350$ , when the flow becomes unsteady. There is a significant increase in swirl strength in the transition of the flow from steady to unsteady state.

The numerical results reveal two distinct bifurcations in the flow states. The flow is steady for small Reynolds numbers ( $Re < 200$ ), while it becomes oscillatory at a Reynolds number of around 250. A predominant frequency and some harmonics are clearly detected ( $St = 1.18$ ) for  $Re = 250$  and ( $St = 1.15$ ) for  $Re = 300$ . By further increasing of the Reynolds number ( $Re > 350$ ), the flow transitions to fully unstable and the velocity oscillations are no longer fundamentally periodic. It is believed that the flow at  $Re = 1000$  may be considered to be the onset of a turbulent

regime. In summary, we have found four different flow regimes in a spacer-filled channel that are laminar-steady ( $Re > 200$ ), laminar-unsteady-periodic ( $Re$  around 300), fully unsteady ( $Re > 300$ ) and onset of turbulent flow ( $Re = 1000$ ).

### Acknowledgements

The authors acknowledge the financial support of the National Research Council of Canada (NRC), the Natural Sciences and Engineering Research Council of Canada (NSERC), and the Program of Energy Research and Development of Natural Resources Canada (PERD). The authors are grateful to Mr. Ron Jerome for technical assistance provided throughout this programme of research.

### References

1. A.R. Da Costa, A. Fane and D. Wiley, "Spacer characterization and pressure drop modelling in spacer-filled channels for ultrafiltration," *Journal of membrane science*, pp. vol.87 iss.1-2 pg.79, 1994.
2. I.S. Kang and H.N. Chang, "The effect of turbulence promoters on mass transfer—numerical analysis and flow visualization," *International Journal of Heat and Mass Transfer*, pp. 25, 1167–1181, 1982.
3. M. Gimmelshtein and R. Semiat, "Investigation of flow next to membrane walls," *Journal of Membrane Science*, pp. 264, 137–150, 2005.
4. J. Santos, V. Geraldes, S. Velizarov and J. Crespo, "Investigation of flow patterns and mass transfer in membrane module channels filled with flow-aligned spacers using computational fluid dynamics (CFD)," *Journal of Membrane Science*, pp. 305, 103–117, 2007.
5. V. Geraldes, V. Semiao and M. de Pinhoa, "Flow management in nanofiltration spiral wound modules with ladder-type spacers," *Journal of Membrane Science*, pp. 203, 87–102, 2002.
6. Z. Cao, D.E. Wiley and A.G. Fane, "CFD simulations of net-type turbulence promoters in a narrow channel," *Journal of Membrane Science*, pp. 185, 157–176, 2001.
7. J. Schwinge, D.E. Wiley and D.F. Fletcher, "Simulation of the Flow around Spacer Filaments between Narrow Channel Walls. 1. Hydrodynamics," *Industrial & Engineering Chemistry Research*, pp. 41, 2977–2987, 2002.

8. S.K. Karode and A. Kumar, "Flow visualization through spacer filled channels by computational fluid dynamics. I: Pressure drop and shear rate calculations for flat sheet geometry," *Journal of Membrane Science*, pp. 193, 69–84, 2001.
9. F. Li, W. Meindersma, A.B. de Haan and T. Reith, "Optimization of commercial net spacers in spiral wound membrane modules," *Journal of Membrane Science*, pp. 208, 289–302, 2002.
10. D.P. Hart, "The elimination of correlation errors in PIV processing," 9th International Symposium on Applications of Laser Techniques to Fluid Mechanics, Lisbon, Portugal, 1998.
11. F. Scarano, M.L. Riethmuller, "Iterative multigrid approach in PIV image processing with discrete window offset," *Experiments in Fluids* pp. 26, 513–523, 1999.
12. Y.L. Li, K.L. Tung, "CFD simulation of fluid flow through spacer-filled membrane module: selecting suitable cell types for periodic boundary conditions," *Desalination*, pp. 233, 351–358, 2008.
13. P. Roache, "Perspective: A method for uniform reporting of grid refinement studies," *ASME Journal of Fluids Engineering*, 116:405 - 413, 1994.
14. S.V. Patankar, C.H. Liu, E.M. Sparrow, "Fully Developed Flow and Heat Transfer in Ducts Having Streamwise-Periodic Variations of Cross-Sectional Area," *ASME Journal of Heat Transfer*, pp. 99:180-186, 1977.
15. J. Ferziger, M. Peric, "Computational Methods for Fluid Dynamics," Chapter 9, 3rd Edition, Springer Verlag, Berlin, 2002.

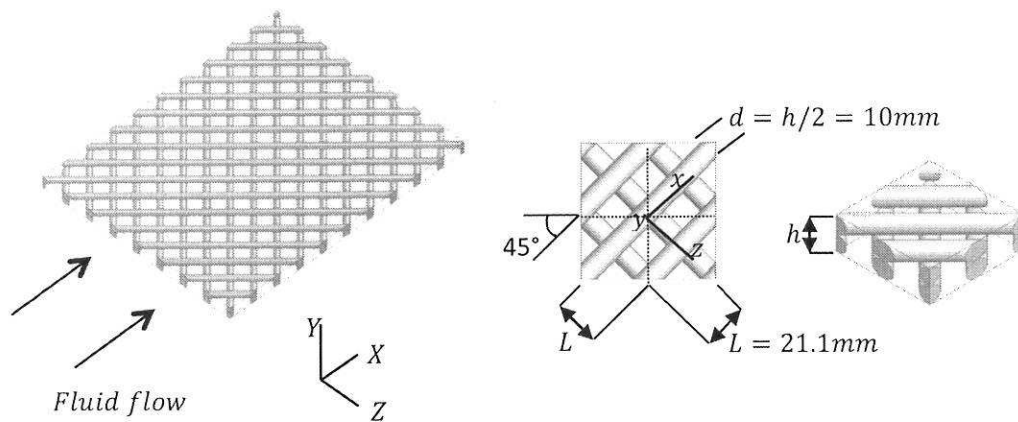


Figure 1: Schematics of the spacer and detail of a  $2 \times 2$  unit cells.

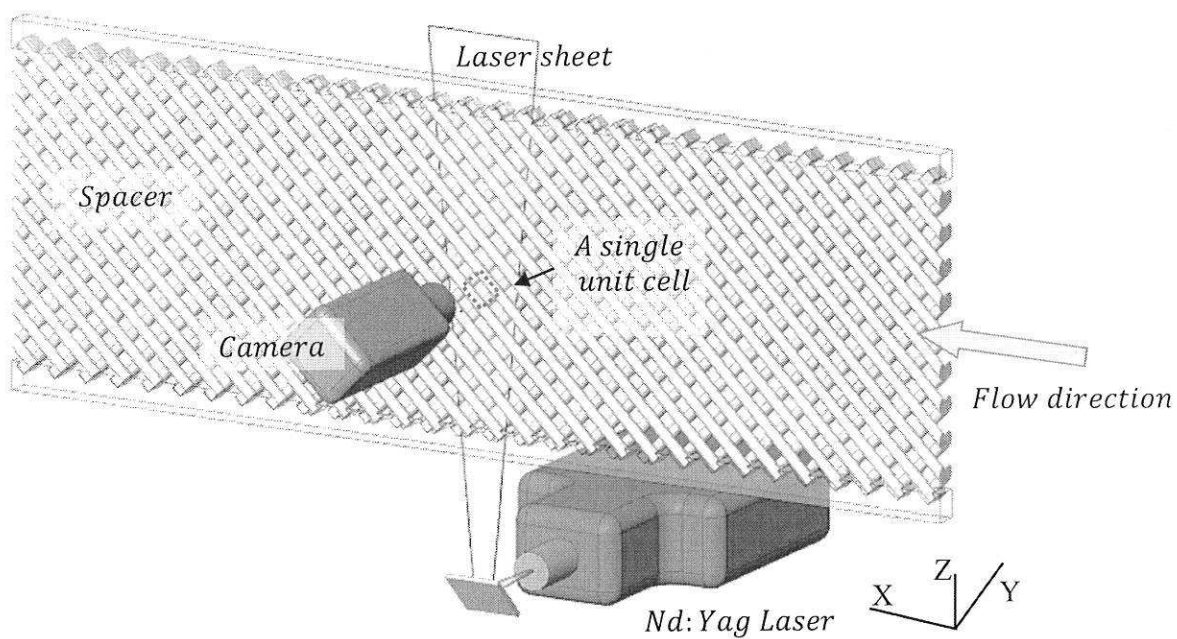


Figure 2: Schematic of the PIV setup. The red dashed area corresponds to the measurement region for a given unit cell. Note that  $Y = 0$  is located in the channel mid-plane.

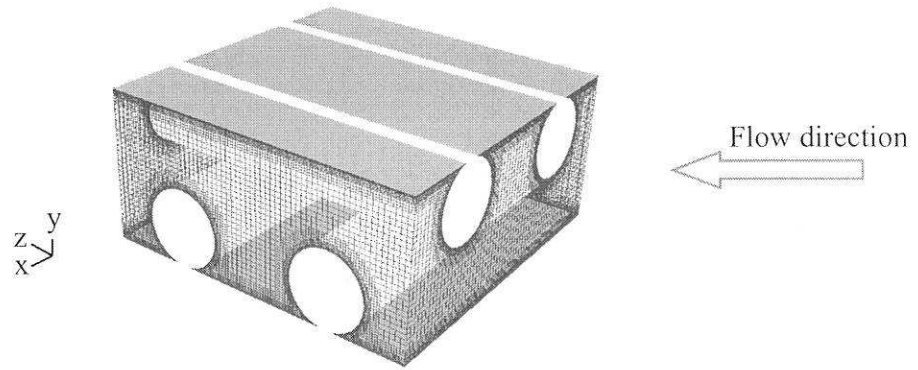


Figure 3: CFD mesh details for unit cell geometry.

Re	$U$ (PIV)	Re	$U$ (PIV)
100		400	
200		500	
300		1000	

Figure 4: Typical instantaneous velocity fields ( $m/s$ ) at  $y = h/4$  from PIV results for various Reynolds numbers. Black dashed lines indicate the location of the spacer filaments boundary at the lower layer of channel ( $y = -h/4$ ). Blue and red indicate slow and fast moving fluid.

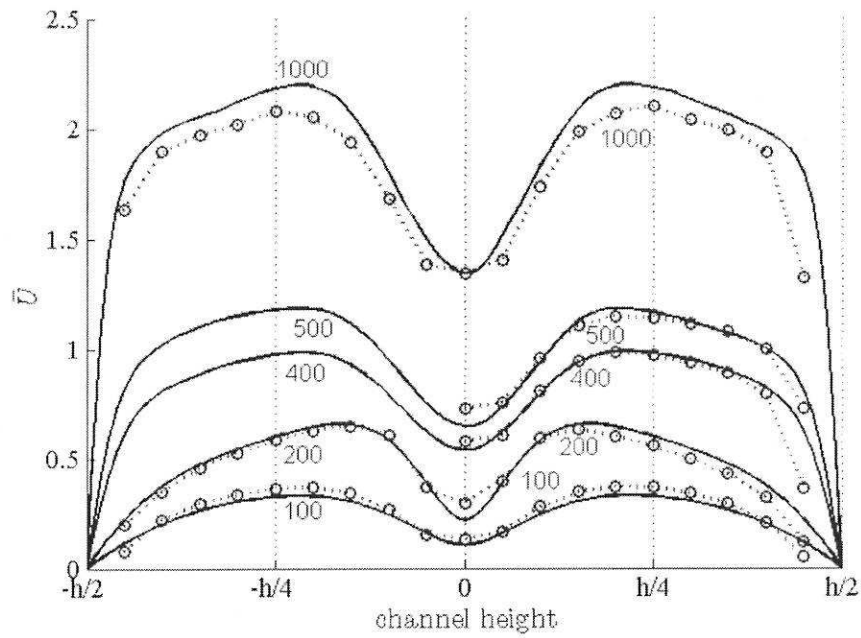


Figure 5: Time-averaged velocity magnitude profiles along line  $x = 0$ ,  $z = 0$  and  $y = -h/2$  to  $h/2$  from CFD (solid line) and PIV (circles) at various Reynolds numbers.



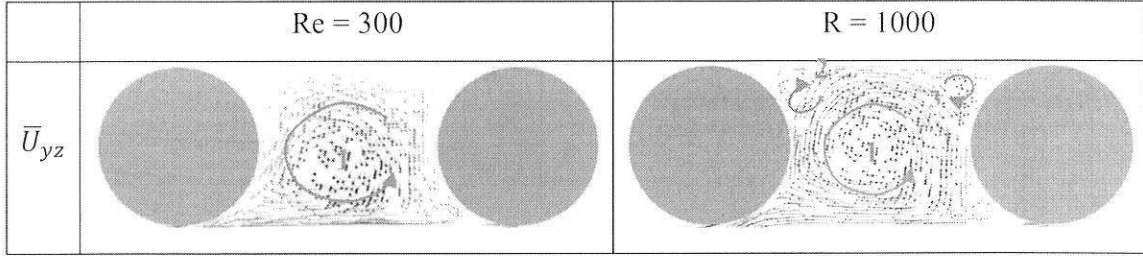


Figure 6: Time-averaged tangential velocity vector plots ( $\bar{U}_{yz}$ ) at plane  $zy$ ,  $x = 0$ ,  $0 < y < h/2$  for  $Re = 300$  and  $1000$ . The red lines indicate the identified vortices.

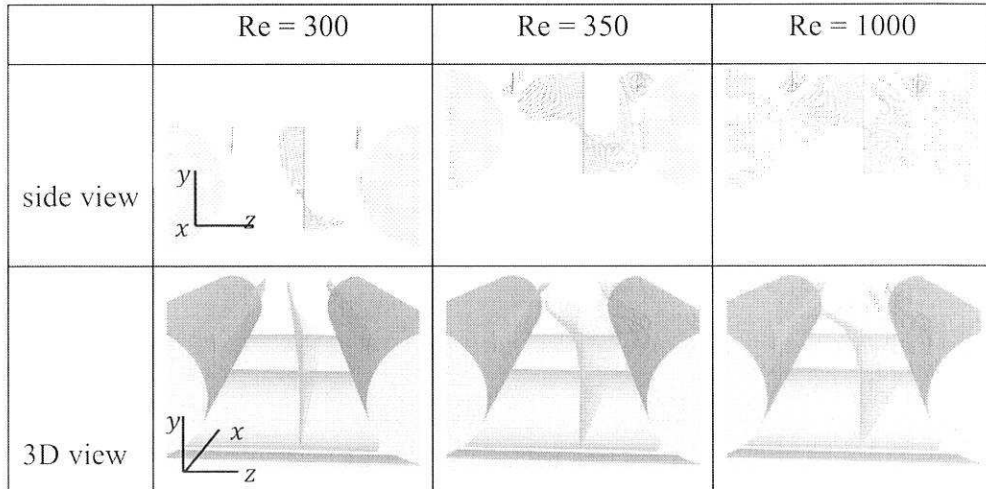


Figure 7: Time-averaged flow streamlines emitted from three lines passed at the swirl centres (indicated in figure 3). Results from DNS.

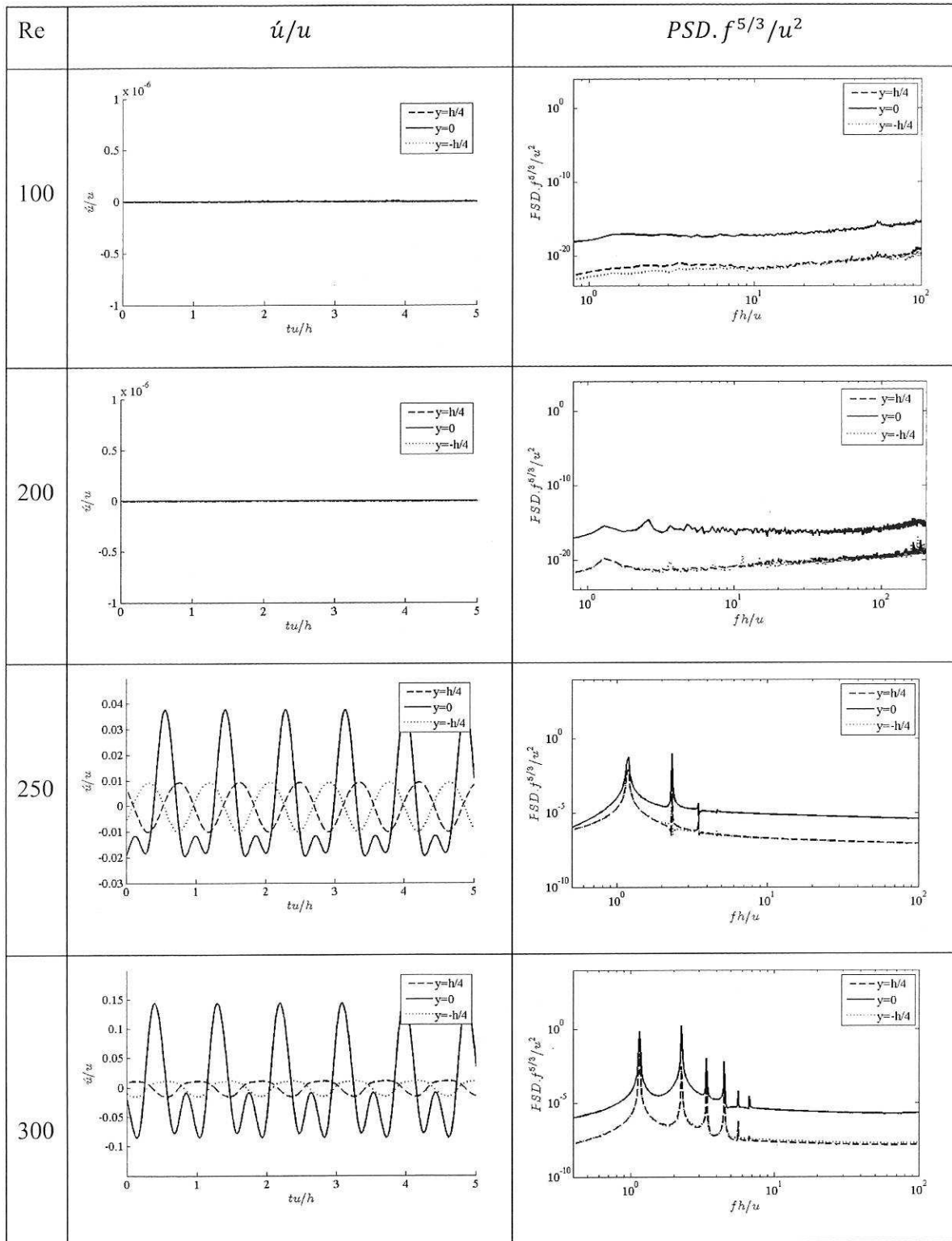


Figure 8(a): History of normalized velocity fluctuation magnitude (left) and normalized compensated power spectral density (PSD) (right) at  $x = 0, z = 0$  and  $y = -h/4, 0, h/4$  for various Reynolds numbers. Results from DNS.

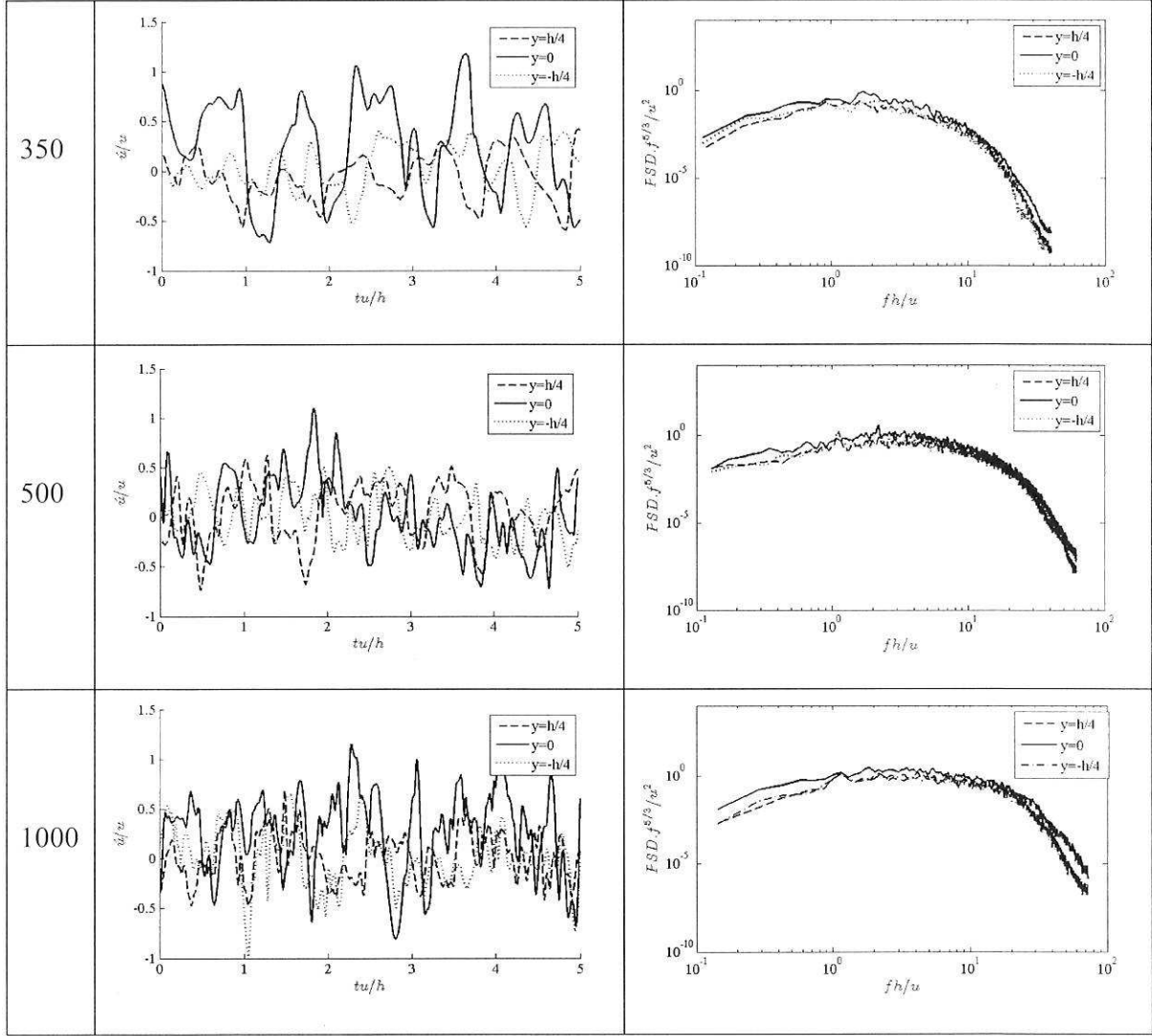


Figure 8(b): History of normalized velocity fluctuation magnitude (left) and normalized compensated power spectral density (PSD) (right) at  $x = 0$ ,  $z = 0$  and  $y = -h/4, 0, h/4$  for various Reynolds numbers. Results from DNS.

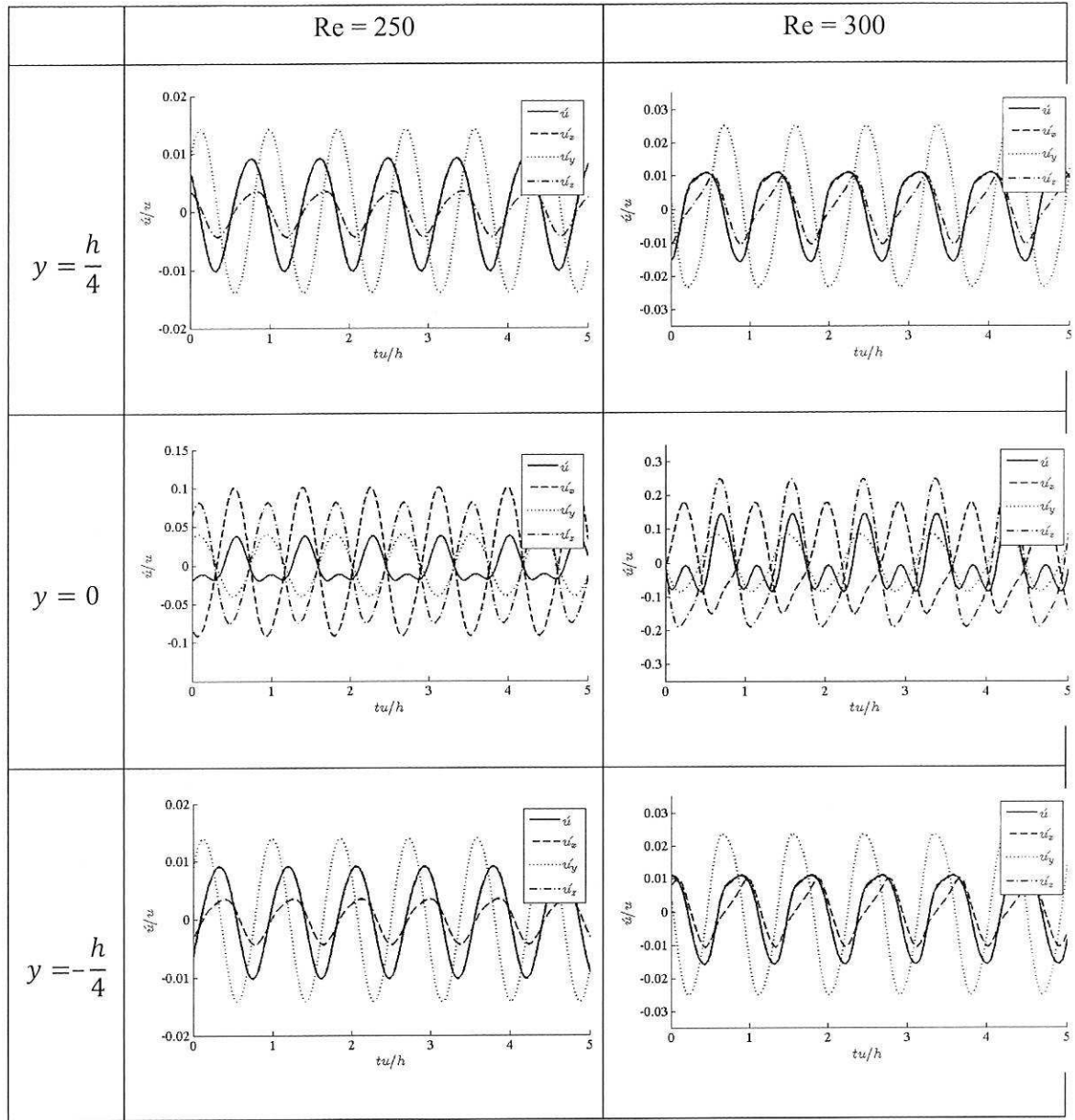


Figure 9: History of normalized fluctuating velocity components and magnitude at three locations ( $x = 0$ ,  $z = 0$  and  $y = -h/4, 0, h/4$ ) for Reynolds numbers 250 and 300. Results from DNS.

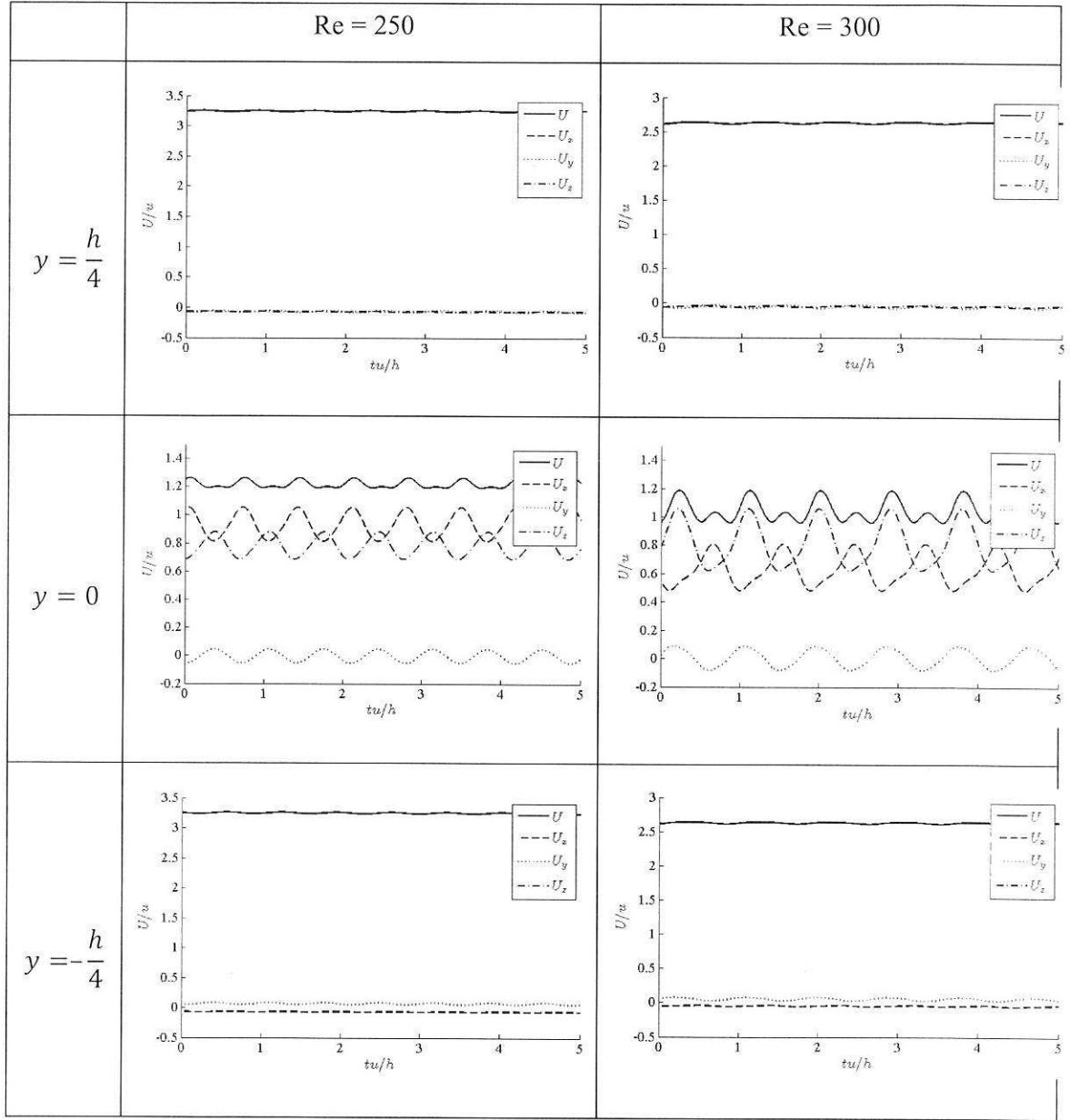


Figure 10: History of normalized mean velocity components and magnitude at three locations ( $x = 0$ ,  $z = 0$  and  $y = -h/4, 0, h/4$ ) for Reynolds numbers 250 and 300. Results from DNS.

